

FABRY-PEROT ABSORPTION-LINE SPECTROSCOPY OF NGC 7079: KINEMATICS AND BAR PATTERN SPEED¹

VICTOR P. DEBATTISTA²

Astronomisches Institut, Universität Basel, Venusstrasse 7, CH-4102 Binningen, Switzerland, and Institut für Astronomie,
ETH Hönggerberg, HPF G4.2, CH-8093, Zurich, Switzerland; debattis@phys.ethz.ch

AND

T. B. WILLIAMS²

Department of Physics and Astronomy, Rutgers, The State University of New Jersey, 136 Frelinghuysen Road, Piscataway, NJ 08854-8019;
williams@physics.rutgers.edu

Received 2003 October 6; accepted 2004 January 7

ABSTRACT

We present Fabry-Perot absorption-line spectroscopy of the SB0 galaxy NGC 7079. This is the first use of Fabry-Perot techniques to measure the two-dimensional stellar kinematics of an early-type disk galaxy. We scan the infrared Ca II line using the Rutgers Fabry-Perot (RFP), to obtain kinematic data extending to I -band surface brightness $\mu_I \simeq 21$ mag arcsec⁻², in a field of radius $\sim 40''$. The kinematic data, consisting of line-of-sight velocities and velocity dispersions, are in good agreement with data obtained along the major axis of the disk with standard slit spectroscopy. Comparison of the exposure times required for slit and RFP spectroscopy to reach the same limiting magnitude shows that the RFP is significantly more efficient for mapping absorption-line galaxy kinematics. We use the velocity data, together with our own deep broadband photometry, to measure the bar pattern speed, Ω_p , of NGC 7079 with the model-independent Tremaine-Weinberg (TW) method. We find $\Omega_p = 8.4 \pm 0.2$ km s⁻¹ arcsec⁻¹; this is the best-constrained pattern speed ever measured for a bar using the TW method. From the rotation curve, corrected for asymmetric drift, we calculate the corotation radius and find that the bar ends just inside this radius. The two-dimensional character of these data allow us to show that the TW method is sensitive to errors in the position angle (P.A.) of the disk. For example, a P.A. error of 2° can give errors $\sim \pm 25\%$ in Ω_p .

Subject headings: galaxies: evolution — galaxies: halos — galaxies: individual (NGC 7079) —
galaxies: kinematics and dynamics — instrumentation: spectrographs

1. INTRODUCTION

Recent experience has demonstrated the utility of integral-field spectroscopy to studies of galaxy dynamics. Verolme et al. (2002), comparing mass models of M32 constrained by integral-field spectroscopy from SAURON (Bacon et al. 2001) and models constrained only by data along four slits extracted from the full two-dimensional data set, found that the mass model parameters, including black hole mass, mass-to-light ratio, and in particular, inclination were substantially better constrained with the full two-dimensional data than with just the slits.

One approach to integral-field spectroscopy is the use of an imaging Fabry-Perot interferometer (FP), essentially a tunable, narrowband filter. The Rutgers Fabry-Perot (RFP), formerly³ at CTIO,⁴ found considerable application to the emission-line study of kinematics and mass modeling of disk galaxies (e.g., Buta & Purcell 1998; Buta et al. 1999, 2001; Beauvais & Bothun 1999, 2001; Palunas & Williams 2000; Weiner et al. 2001a; Weiner, Sellwood, & Williams 2001b). However, FP stellar absorption-line spectroscopy in galaxies

is significantly more difficult because of the lower surface brightness levels, the shallowness and width of the spectral features, and the effects of time-variable observing conditions on reconstructing line profiles necessarily sampled sequentially over an extended period of observation. Because of these difficulties, FP stellar absorption-line spectroscopy has not been previously successfully attempted in galaxies, although absorption-line spectroscopy of individual stars in globular clusters has been accomplished with considerable success (Gebhardt et al. 1994, 1995, 1997). In this paper we study the kinematics of a bright, barred, disk galaxy with stellar absorption-line spectroscopy using the RFP, which is well-suited to galactic spectroscopy because of its large field-of-view, high throughput, and appropriate spectral resolution ($R = \lambda/\delta\lambda \simeq 2000$).

More than half of all high surface brightness disk galaxies are barred (Knapen 1999; Eskridge et al. 2000). The fundamental parameter in the dynamics of barred galaxies is the pattern speed of the bar, Ω_p . This is usually expressed in terms of the quantity $\mathcal{R} = D_L/a_B$; here a_B is the length of the semimajor axis of the bar and D_L is the Lagrangian/corotation radius, where, in the bar's rest frame, the centrifugal and gravitational forces balance. A self-consistent bar with orbits aligned with the bar has $\mathcal{R} \geq 1$ (Contopoulos 1980); when $1.0 \leq \mathcal{R} \lesssim 1.4$, a bar is termed fast.

Because bars have strong quadrupole moments, they lose angular momentum efficiently in the presence of a dense dark matter (DM) halo, as first shown by perturbation theory

¹ Based in part on observations carried out at the European Southern Observatory (Prop. B-0329).

² Visiting Astronomer, Cerro Tololo Inter-American Observatory (CTIO).

³ The RFP has since been decommissioned. Replacement by the next generation RFP is scheduled for 2004.

⁴ The Cerro Tololo Inter-American Observatory (CTIO) is part of The National Optical Astronomy Observatories (NOAO), which are operated by the Association of Universities for Research in Astronomy (AURA) Inc., under cooperative agreement with the National Science Foundation.

calculations (Weinberg 1985). Early simplified simulations (Little & Carlberg 1991, Hernquist & Weinberg 1992) found agreement with Weinberg’s calculations. The presence of DM in disk galaxies is required by their rotation curves, which stay flat out to large radii (Rubin, Ford, & Thonnard 1980; Bosma 1981). Determining the relative amounts of luminous and dark matter in the region of the optical disk, however, is a difficult problem, because of degeneracy in the contributions of the two components to the rotation of axisymmetric systems. The maximum disk hypothesis (van Albada & Sancisi 1986), which requires the maximum amount of disk matter consistent with the inner rotation curve, often accounts for the shapes of the rotation curves of high surface brightness (HSB) galaxies (e.g., Kalnajs 1983; Kent 1986; Corsini et al. 1999; Palunas & Williams 2000). Others studies, however, have argued that maximum disks cannot account for other observational properties (e.g., van der Kruit 1995; Bottema 1997; Courteau & Rix 1999, Kranz, Slyz, & Rix 2001). Debattista & Sellwood (1998) realized, from fully self-consistent simulations, that fast bars require that barred galaxies have maximum discs. At present, there is a lively debate about this suggestion (Tremaine & Ostriker 1999; Debattista & Sellwood 2000; Weinberg & Katz 2002; Valenzuela & Klypin 2003; O’Neill & Dubinski 2003).

One of the issues surrounding this debate concerns just how rapidly bars rotate. The number of barred galaxies in which \mathcal{R} has been measured is still relatively small. Evidence that bars are fast comes mostly from simulations of the hydrodynamics of gas in the bar region (e.g., Athanassoula 1992; Lindblad, Lindblad, & Athanassoula 1996). The example of NGC 4123 (Weiner et al. 2001b) is especially instructive because the hydrodynamical simulations require both a fast bar and a maximum disk to match the observed gas shocks. A direct (model-independent) method for measuring bar pattern speeds was devised by Tremaine & Weinberg (1984). The Tremaine-Weinberg (TW) method is contained in the following simple equation:

$$\mathcal{X}\Omega_p \sin i = \mathcal{V}. \quad (1)$$

Here $\mathcal{X} = \int h(Y)X\Sigma dX dY$, $\mathcal{V} = \int h(Y)V_{\text{los}}\Sigma dX dY$, Σ is the surface brightness, $h(Y)$ is an arbitrary weighting function, V_{los} is the line-of-sight velocity, i is the disk inclination (throughout, we use the convention $i = 0$ for face-on), and (X, Y) are galaxy-centered coordinates measured along the disc’s apparent major and minor axes, respectively. Although the integrals in \mathcal{X} and \mathcal{V} range over $-\infty \leq X \leq \infty$, if the disk is axisymmetric at $|X| \geq X_o$, then integration over $-X_o \leq X \leq X_o$ suffices. The integration in Y is over an arbitrary range, because of $h(Y)$; for example a weight function proportional to a delta function corresponds to a slit parallel to the disk major axis. For a number of such slits, plotting \mathcal{V} against \mathcal{X} gives a straight line with slope $\Omega_p \sin i$. The TW method has previously been applied to a handful of galaxies, all with slit data (Merrifield & Kuijken 1995; Gerssen, Kuijken, & Merrifield 1999, 2003; Debattista et al. 2002; Aguerri, Debattista, & Corsini 2003). In all cases, bars were found to be consistent with $1.0 \leq \mathcal{R} \leq 1.4$. However, TW measurements are technically challenging, and in some cases large uncertainties result. Thus, for example, Valenzuela & Klypin (2003) argue that $R = 1.7$, which they find in their simulations, is still consistent with observations. While correct, this claim overlooks the fact that this limit is reached only in those galaxies with the largest uncertainties (Aguerri et al. 2003, hereafter ADC03) and ignores other

sources of scatter (Debattista 2003, hereafter D03). There exists, therefore, a need for at least a few high-precision measurements of \mathcal{R} .

Integral field velocity data permit TW measurements of Ω_p with greater precision, because of the improved spatial coverage. In this paper we present observations of NGC 7079 using the RFP interferometer, which allowed us to measure two-dimensional kinematics down to a surface brightness $\mu_l \sim 21$ mag arcsec⁻². In § 2 we describe NGC 7079, emphasizing those properties that make it a suitable system for this analysis. In § 3 we present photometry of NGC 7079. This is the first use of the RFP for absorption-line spectroscopy of galaxies, and therefore in § 4 we present the spectroscopy and reduction methods. We show that the resulting data are in good agreement with data obtained by standard slit spectroscopy. In § 5 we study the kinematics of NGC 7079 and measure Ω_p with the TW method. We show at this point that the measured Ω_p is quite sensitive to small errors in the position angle (P.A.) of the disk. Finally, in § 6 we discuss our results and conclusions.

2. NGC 7079

In choosing candidates for observation, SB0 galaxies were selected from various catalogues and examined in the Digitized Sky Survey.⁵ Candidates were chosen with a bar at a position angle intermediate between the minor and major axes of the disk (as required by the TW method), a number of bright stars within 80'' of the galaxy center (to permit determination of temporal atmospheric transmission variations between the RFP frames) and lacking strong spirals, patchy dust, and significant companions. The galaxies needed to be bright and large and have known recession velocities (required for efficient use of the RFP). Finally, we chose to use the Ca II 8542.09 Å absorption line because it is quite strong, and the combination of the red color of SB0 galaxies and the moderately high CCD detector quantum efficiency in this portion of the spectrum maximizes the measurement efficiency here. Since this region of the spectrum contains a host of night-sky emission features (see Osterbrock et al. 1996), we selected candidate galaxies with redshifts that placed the Ca II line in relatively emission-free regions.

NGC 7079 (ESO 287–36) satisfied all these conditions. NGC 7079 is classified as (L)SB(r)0⁰ (Buta 1995), is large and bright (2.3×1.3 , $B_T = 12.46$; de Vaucouleurs et al. 1991, hereafter RC3) and has a measured recession velocity (2670 ± 25 km s⁻¹; Lauberts & Valentijn 1989). The redshifted wavelength of the Ca II line is therefore 8618 Å; assuming a rotation velocity of about 260 km s⁻¹ (Bettoni & Galletta 1997) and allowing for the width of the Ca II stellar line and for the gradient in wavelength across the RFP frame, we needed to scan the galaxy from 8608 to 8631 Å. The sky has no emission between 8598 and 8613 Å and some weak O₂ emission (which can be subtracted out) between 8613 and 8631 Å. Bettoni & Galletta (1997) detected O [III] $\lambda = 5007$ Å emission extending out to $\sim 15''$, but this gas is faintly emitting and is not expected to affect measurement of Ω_p . NGC 7079 is the brightest member of a group containing seven galaxies (Garcia 1993), but the nearest large neighbor, ESO 287–37, is over 0°.5 away from it, or 363 kpc (in projection) at a distance of 38 Mpc (we assume throughout this

⁵ The Digitized Sky Survey was produced at the Space Telescope Science Institute (STScI) and funded by the National Aeronautics and Space Administration.

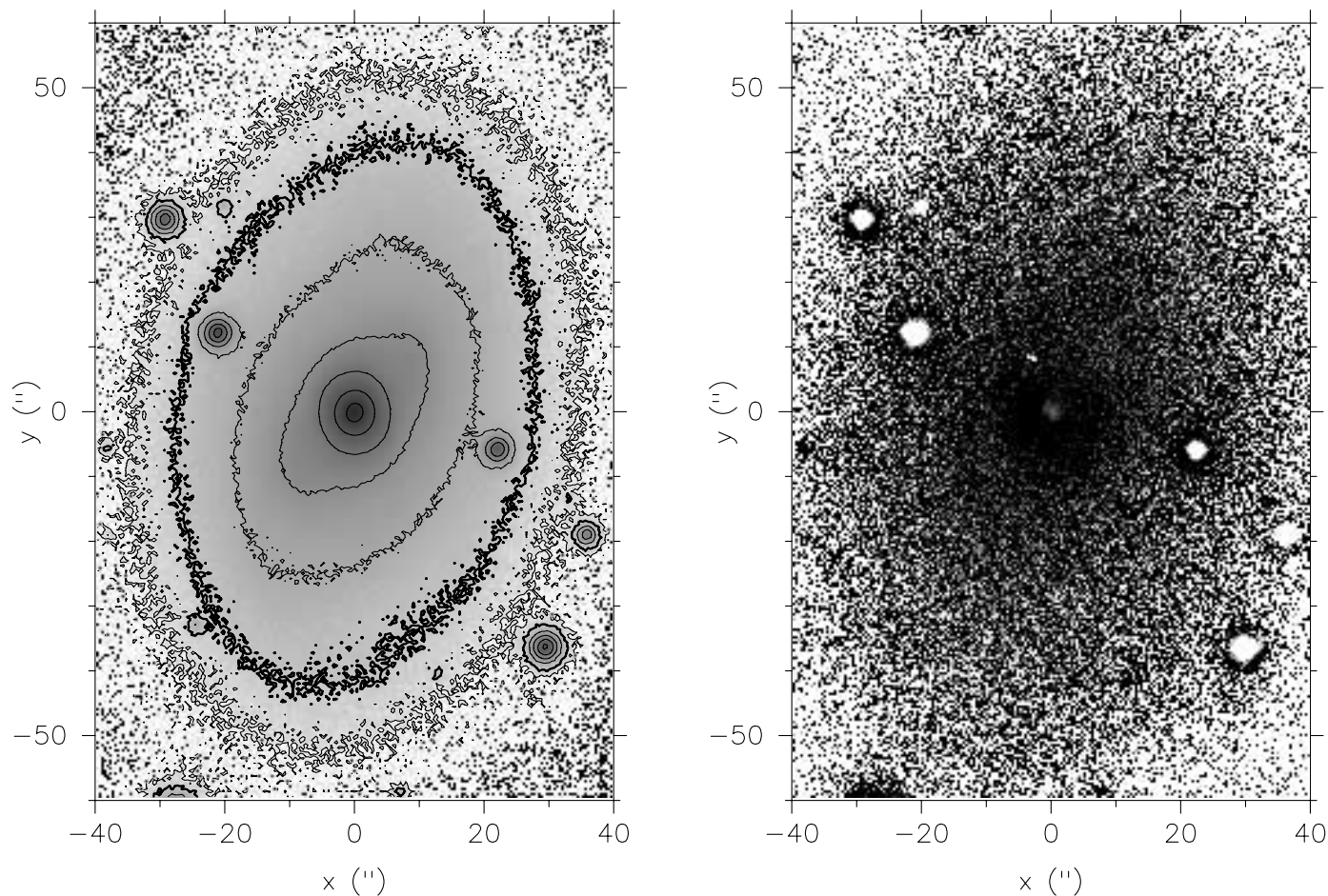


FIG. 1.—*I*-band (left) and the *B*–*I* maps (right) of NGC 7079. North is left, and west is up in each panel. The bright stars near the galaxy were used to normalize the RFP frames. The contours in the *I*-band map are spaced at 1 mag arcsec⁻², with the bold contour indicating $\mu_I = 21$ mag arcsec⁻². The only significant feature in the color map is the bulge at the center, with no evidence for a patchy obscuration.

paper that $H_0 = 70$ km s⁻¹ Mpc⁻¹). The other group members are more than twice as far away, so we expect that NGC 7079 should not be significantly perturbed.

3. SURFACE PHOTOMETRY

3.1. Observations and Reduction

We obtained deep images of NGC 7079 at the CTIO 0.9 m telescope on the night of 1997 August 2–3 under photometric conditions. We used the TeK 2K No. 3 CCD in quad readout mode, with a gain of $3.3e^-$ ADU⁻¹ and read noise of $4.7e^-$ averaged over the four quadrants. The image scale in this configuration was $0''.396$ pixel⁻¹, for an unvignetted field of 13.5×13.5 . The exposure time for each image of the galaxy was 900 s; we acquired four exposures in *I*, two each in *B*, *V*, and *R*, and one exposure in *U*. The seeing through the night was $\sim 1''.5$. For the *I*-band images, the telescope was moved between exposures so that the galaxy's image fell on different parts of the CCD, to allow the effects of bad pixels to be removed when the images were combined. The images were flat-fielded with twilight sky flats and zero-subtracted as usual. Using the IRAF⁶ task *imalign*, the *I*-band images were shifted to the nearest pixel and then combined using the biweight, a

robust statistical estimator of the mean that is insensitive to outliers (Beers et al. 1990). (Because of the small pixel scale relative to the seeing, integer pixel shifts were adequate and avoided interpolation effects around image artifacts.) A constant sky value, obtained from image regions that were free of stars and galaxy light, was subtracted from each image. All were then cleaned of cosmic rays using IRAF's task *cosmic-rays*. The resulting *I*-band image is shown in Figure 1. A *B*–*I* map, also shown in Figure 1, reveals little structure apart from a nucleus bluer than the disk, indicating that there is no variable obscuration within the galaxy (as required for the TW method).

Two standard stars were used for calibration, E9-47-U and E1-44-S (Graham 1982). We obtained the values of the Galactic extinction from Schlegel et al. (1998) via NED.⁷ We did not measure the differential atmospheric extinction, but used the standard value from Hamuy et al. (1992). Since we observed NGC 7079 and the standard stars all at less than 1.1 air masses, the resulting uncertainties are insignificant for our purposes.

3.2. Isophotal Analysis

After masking bad pixels, foreground stars, and all pixels outside $100''$ from the galaxy center, we fitted ellipses, with

⁶ IRAF is distributed by NOAO, which is operated by AURA Inc., under contract with the National Science Foundation.

⁷ The NASA/IPAC Extragalactic Database (NED), is operated by the Jet Propulsion Laboratory, California Institute of Technology, under contract with the National Aeronautics and Space Administration.

fixed centers, to single U , B , V and R -band images and to the combined I -band image, using the IRAF task *ellipse*. We determined integrated magnitudes using the fitted ellipses and IRAF's task *bmodel*. We do not correct these magnitudes for the galaxy's inclination. Our results are reported in Table 1, along with the total asymptotic U , B , and V aperture-magnitudes given in RC3. Our magnitudes for NGC 7079 are a bit fainter than RC3, possibly because we masked out the bright stars in the vicinity of the galaxy and have not extrapolated the profiles to infinity. To measure the colors, we again used the task *ellipse*, but now constrained to measure the photometry in the same ellipses as were fitted to the I -band, so that magnitudes can be meaningfully compared in the same regions. The results are plotted in Figure 2. Apart from the slightly bluer nucleus, the color profile is remarkably flat, with barely detectable color gradients.

We fitted separate exponential disks to the photometry in B , V , R , and I in the radial range $25'' < R < 40''$, finding an average scale-length, R_d , of $17''.1 \pm 2''.0$ (corresponding to 3.1 ± 0.4 kpc at our assumed distance) and $\mu_{0,B} = 20.5$ mag arcsec $^{-2}$. The latter value deprojects to 21.0 mag arcsec $^{-2}$, close to the Freeman (1970) limit (21.65 ± 0.3 mag arcsec $^{-2}$). At $R \gtrsim 45''$, the surface brightness profile steepens. This break radius remained unchanged when we fitted ellipses after changing the constant sky background level by $\pm 1 \sigma$, and it is identical for B , V , R and I bands, despite a difference in sky background level of 3 mag. We conclude, therefore, that the break in the surface brightness is not an artifact of imperfect sky subtraction. Sharp disk truncations have been noted in photographic plate studies (van der Kruit 1979), while in a large sample of edge-on galaxies, Pohlen et al. (2002) found radial structure that is better fitted by two exponentials than by sharply truncated exponentials. His break radii ($R_b/R_d = 2.5 \pm 0.8$) and surface brightnesses at R_b ($\mu_R = 22.6 \pm 0.6$ mag arcsec $^{-2}$) agree well with the values we obtain for the break in NGC 7079 (2.6 and 22.0, respectively). While the fact that R_b is identical in all bands argues forcefully that this is a real structure, it is clear that the disk profile continues past R_b (see Narayan & Jog 2003).

We use data at semimajor axis larger than $51''.5$ to calculate the median values of the disk ellipticity, ϵ_{disk} , and P.A. $_{\text{disk}}$. Figure 3 shows these results averaged over all colors. We find $\epsilon_{\text{disk}} = 0.36 \pm 0.02$ corresponding to an inclination $i = 49^\circ.8 \pm 1^\circ.7$ for a razor-thin disk. If, however, the ratio of disk scale height to scale length is $q_0 = 0.2$, we use the standard equation (Hubble 1926) $\cos i = [(b^2/a^2 - q_0^2)/(1 - q_0^2)]^{1/2}$, to obtain $i = 51^\circ.3$. We therefore adopt $i = 50^\circ.6 \pm 2^\circ.3$, which is in good agreement with RC3 ($i = 51^\circ.8$). Our value of P.A. $_{\text{disk}} = 78^\circ.8 \pm 0^\circ.1$; the RC3 value for this parameter is 82° .

Since a bar represents an $m = 2$ perturbation of the disk density, a Fourier decomposition of the deprojected surface

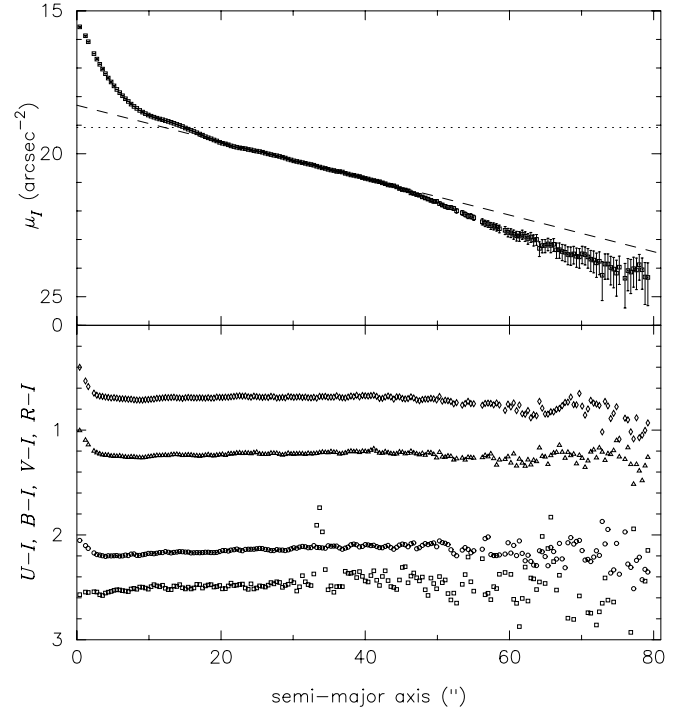


FIG. 2.—*Top*: Sky-plane surface brightness of NGC 7079 in the I band. The sky level is indicated by the dotted horizontal line, while the dashed line indicates the best-fit exponential within $25'' < R < 40''$. The radial profile exhibits a break at $\sim 45''$ ($\mu_I \simeq 21.2$ mag arcsec $^{-2}$). *Bottom*: The colors of NGC 7079. The squares are $U-I$, the circles $B-I$, the triangles $V-I$ and the diamonds $R-I$. Note the quite flat colors (contamination by scattered light in the U band is responsible for the feature seen in $U-I$ between $30''$ and $35''$).

density is well suited to measuring the semimajor axis of the bar, a_B . Since two independent parameters, an amplitude and a phase, define each $m \neq 0$ harmonic, two independent estimates of a_B are possible from a Fourier decomposition. Our first estimate of a_B , based on amplitudes, is given by the

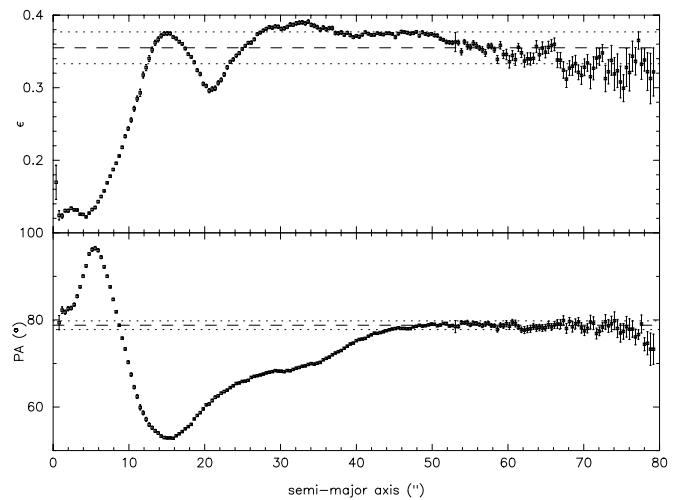


FIG. 3.—Sky-plane ellipticity (*top*) and P.A. (*bottom*) of NGC 7079. The data from the ellipse fits to the U , B , V , R , and I bands have been averaged together for this figure. The disk's ellipticity and P.A. are determined from data with semimajor axis larger than $51''.5$. This gives $\epsilon_{\text{disk}} = 0.36 \pm 0.02$ and P.A. $_{\text{disk}} = 78^\circ.8 \pm 0^\circ.1$. The average values of ϵ_{disk} and P.A. $_{\text{disk}}$ are shown by the dashed lines; the standard error on ϵ_{disk} is shown by the dotted lines, while the dotted lines in the bottom panel show P.A. $_{\text{disk}} \pm 1^\circ$, illustrating that P.A. $_{\text{disk}}$ can be determined to better than 1° from these data.

TABLE 1
APPARENT MAGNITUDES OF NGC 7079

Filter	m	m_T^a
U	13.2	12.83 ± 0.13
B	12.6	12.46 ± 0.13
V	11.7	11.59 ± 0.13
R	11.1	...
I	10.4	...

NOTE.—We estimate that our uncertainty is less than 0.1 mag in all bands.

^a RC3 (via NED).

method of Aguerri et al. (2000), which has been used in other early-type barred galaxies (Debatista et al. 2002; ADC03). The method defines a_B as the radius for which $(I_b/I_{ib}) = (I_b/I_{ib})_{1/2} \equiv 0.5[(I_b/I_{ib})_{\max} + (I_b/I_{ib})_{\min}]$, where $I_b = 1 + A_2$, $I_{ib} = 1 - A_2$ and A_2 is the amplitude of the $m = 2$ Fourier component, normalized by that of $m = 0$. For NGC 7079 this prescription gives $a_B = 28''.9$. For a phase-based estimate of a_B , we deprojected the ellipse fits and measured the phase angle of the resulting ellipses. The value of a_B is then the largest radius out to which the phases are consistent with a constant, taking into account that deprojecting the bulge, which we did not subtract from our image for this analysis, results in a twist interior to the bar. We found $a_B = 21''.9$ this way; we therefore adopt $a_B = 25''.4 \pm 3''.5$. Figure 4 presents the bar-length analysis and also shows that ψ_{bar} , the bar angle in the intrinsic galaxy frame as measured from the major axis of the disk, is $\simeq 58''.5$, which projects to $\text{P.A.}_{\text{bar}} = 32''.8$.

4. SPECTROSCOPY

4.1. Observations and Reduction

We observed NGC 7079 on 1997 July 28 with the CTIO 4 m telescope using the RFP imaging interferometer and the TeK 2K number 6 CCD. The instrument has a circular field of view of radius $\sim 85''$, and the detector was operated with 2×2 pixel binning, producing an image scale of $0''.70 \text{ pixel}^{-1}$. The detector gain and read noise were $1.0 \pm 0.1 e^- \text{ ADU}^{-1}$ and $2.9 \pm 0.2 e^-$, respectively. We used the ‘‘broad’’ RFP etalon, with a resolution FWHM $\sim 4.2 \text{ \AA}$ (150 km s^{-1}) and free spectral range of $\sim 100 \text{ \AA}$ at the Ca II line. The spectral instrumental profile of the RFP is well fitted by a Voigt profile, the convolution of a Lorentzian and a Gaussian of widths $\sigma_l = 1.93 \text{ \AA}$ and $\sigma_g = 0.45 \text{ \AA}$, respectively. We used a blocking filter of FWHM 100 \AA to select the desired spectral order. The wavelength calibration of the RFP was determined with a precision of $\sim 0.04 \text{ \AA}$. Because the wavelength zero point and the optical center drift during the night (owing to flexure, temperature changes, etc.), we took additional

calibration measurements hourly through the night and incorporated these corrections in the data reductions. We found average drift rates of $0.086 \text{ \AA hr}^{-1}$ and $0.36 \text{ pixels hr}^{-1}$ for the zero point and the optical center, respectively. The temperature dropped during the night, until the telescope primary mirror was some 2.5°C warmer than the ambient air, producing poor seeing of $1''.6\text{--}3''.0$ (FWHM). There were also strong winds, reaching 50 mph by morning, and the night was nonphotometric, with thin variable cloud. Nevertheless, we managed to obtain 24 exposures of 900 s each, spanning the wavelength range $8608\text{--}8631 \text{ \AA}$ in steps of $\sim 1 \text{ \AA}$ (35 km s^{-1} at 8618 \AA). We first stepped through the full wavelength range in steps of $\sim 2 \text{ \AA}$ and then filled in the intermediate wavelengths with a second scan (one wavelength sample was inadvertently repeated).

The images were zero subtracted and flat-field-corrected (with the median of three dome flats at each wavelength) in the usual way. Cosmic rays were then cleaned by replacement using IRAF. In an imaging FP, the transmitted wavelength varies quadratically with the distance from the optical axis; for the RFP at Ca II the field is $\sim 7.5 \text{ \AA}$ bluer at the outer edge than on the optical axis. Thus the sky background in each frame varies radially as a result of the spectral energy distribution of the night sky. We offset NGC 7079 to the right half of the field of view, so that we could determine the sky spectrum from the left half of the field. Because some faint galaxy light from the outer disk does reach to the left side of the frames, as well as a ghost image from reflections off the CCD and FP, we developed an iterative scheme to determine and subtract the sky. Briefly, the initial estimate of the sky spectrum was determined from the left half of the image and subtracted from the entire image; this approximately sky-free image was used to estimate and remove the contributions of the outer galaxy and the ghost reflection from the left half of the original image, leading to an improved estimate of the sky spectrum. A second iteration of this procedure produced the final sky spectrum that was subtracted from the images.

The images were then masked, shifted to a common frame, and convolved with a radially symmetric Gaussian to a common seeing. We did this twice, once for all 24 images, (seeing FWHM = $2''.6$) and again for the best 18 images, excluding those obtained under poor conditions at the end of the night (resulting FWHM = $2''.2$). Since the atmospheric transparency varied by $\sim 12\%$ during the night, all images needed to be normalized to a common transparency. We determined the normalization coefficients by measuring the flux of seven bright stars in our field and assuming that their mean spectrum over our wavelength range was flat and featureless. Finally, we generated noise maps that include photon, sky and read noise, and that account for the Gaussian and image registration smoothings.

To determine the kinematic properties of NGC 7079, we fitted a Voigt profile to the spectral data at each spatial position in the FP data cube. The data to be fitted were smoothed with box car averaging using an adaptive kernel ranging from 1×1 to 7×7 pixels based on the flux level, and the fits were weighted by the inverse square of the estimated flux uncertainties. The parameters of the fit were the continuum level, the line strength, the line-of-sight velocity, and the Gaussian velocity dispersion; maps of these quantities and their uncertainties were produced. We were able to obtain reliable fits within an ellipse of semimajor axis length of $\simeq 40''$ ($\mu_l \simeq 21 \text{ mag arcsec}^{-2}$). We did not attempt to fit higher velocity moments, such as the Gauss-Hermite moments h_3 and h_4

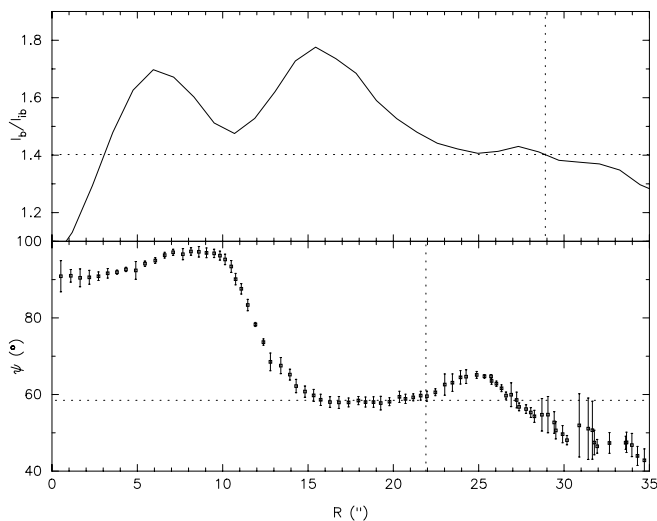


FIG. 4.—*Top*: Estimate of a_B based on the amplitudes of the Fourier $m = 2$ deprojected moment. The dotted horizontal line shows the value of $(I_b/I_{ib})_{1/2}$, from which $a_B = 28''.9$, indicated by the vertical dotted line, is obtained. *Bottom*: The deprojected position angles relative to $\text{P.A.}_{\text{disk}}$, ψ , of the ellipse fits of Fig. 3 (averaged over all bands) in the inner part of the galaxy. The vertical dotted line is at $a_B = 21''.9$. The horizontal dotted line shows $\psi_{\text{bar}} \simeq 58''.5$.

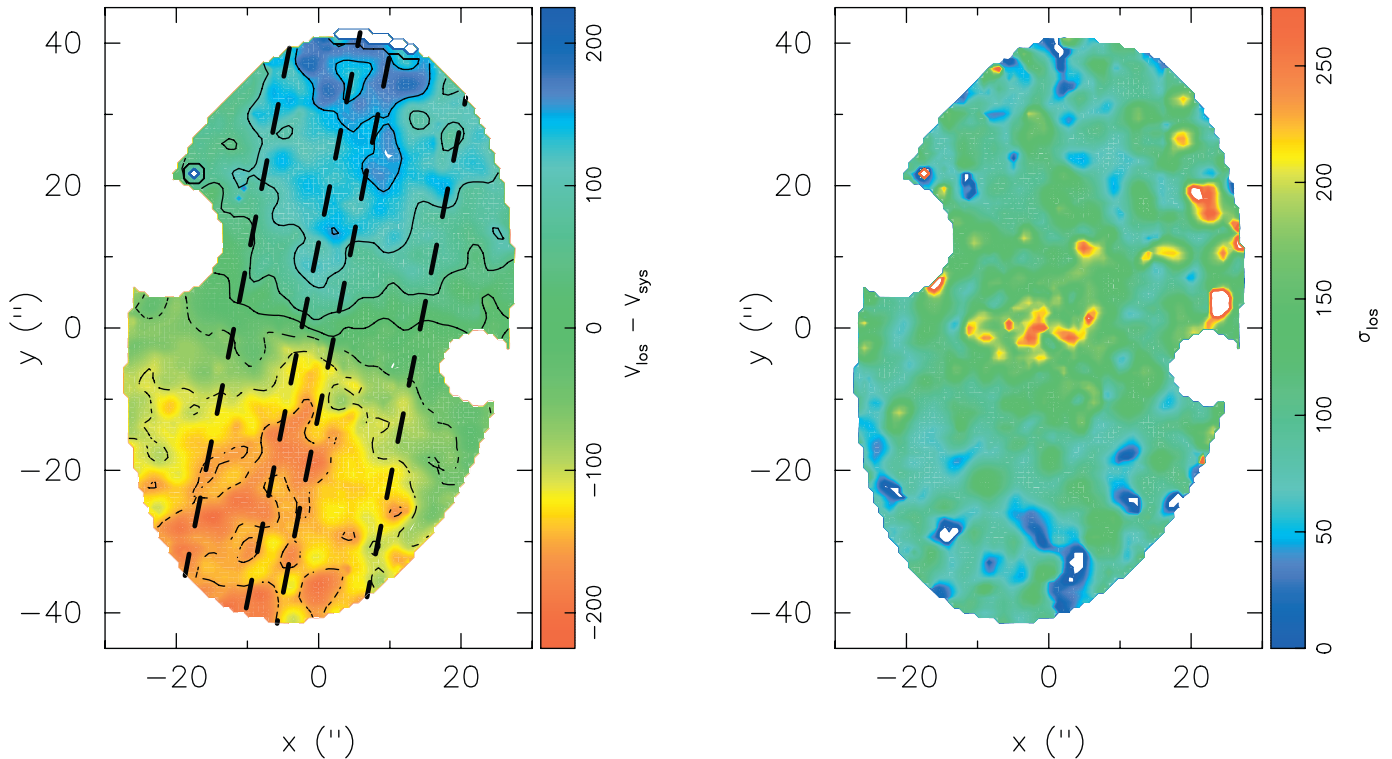


FIG. 5.—Line-of-sight velocity (*left*) and velocity dispersion (*right*) fields; north is left, and west is up. In the velocity panel, contours are spaced by 50 km s^{-1} , centered on the systemic velocity and are solid (dashed) lines on the approaching (receding) side. The bold dashed lines in the velocity panel indicate the two regions within which we applied the TW analysis. Our limits on large $|Y|$ were chosen to avoid contamination by starlight, and the limits on small $|Y|$ are intended to avoid a small offset in the kinematic center.

(Gerhard 1993; van der Marel & Franx 1993). A comparison of the velocity fits produced from the 18 and 24 image data cubes showed no significant differences, mostly because of the poor quality of the last six images; in the following, therefore, we consider only the fits based on the better seeing (18 image) data cube.

Figure 5 presents the resulting velocity and velocity dispersion maps. Other than a slight S distortion in the central regions due to the bar, the velocity distribution is that expected for an inclined, rotating disk. The velocity dispersion is largest in the nucleus and bulge, lower along the bar, and smallest in the disk. Examples of fitted profiles are presented in Figure 6; these show successful fits from the galaxy center (panel 3) to $\mu_I = 21 \text{ mag arcsec}^{-2}$ (panels 1 and 7). By $\mu_I = 22 \text{ mag arcsec}^{-2}$, the signal-to-noise ratio is too low and only the noise is fitted (panel 12). The spectrum of one of the foreground stars (panel 10) is essentially constant (with possibly a very weak Fe $\lambda 8611$ line). As seen in panel 3, the FP scan did not extend far enough in wavelength to sample the continuum adequately in the high velocity dispersion regions in the center of the galaxy; thus while the velocities are well determined here, the velocity dispersion measurements have larger systematic uncertainties.

4.2. Comparison with Slit Spectroscopy

Since this is the first application of the RFP to absorption-line spectroscopy of galaxies, it is important to confirm that our results agree with those obtained by traditional slit spectroscopy. For this purpose, E. M. Corsini kindly obtained and reduced for us a long-slit spectrum along the major axis of NGC 7079. The 1800 s exposure was taken in 16 November 2001 using the ESO New Technology Telescope (NTT) with EMMI in red medium-dispersion spectroscopic mode and using

the grating No. 6 with $1200 \text{ grooves mm}^{-1}$ in first order with a $1''.0 \times 5''.5$ slit. The detector was the No. 36 Tektronix TK2048 EB CCD with $2048 \times 2048 \text{ } 24 \mu\text{m}$ pixels. It yielded a wavelength coverage between about 4840 and 5490 \AA with a reciprocal dispersion of $0.320 \text{ \AA pixel}^{-1}$. The instrumental resolution was 1.19 \AA (FWHM) corresponding to $\sigma_{\text{inst}} \approx 30 \text{ km s}^{-1}$ at 5170 \AA . The spatial scale was $0''.270 \text{ pixel}^{-1}$.

The spectrum was bias-subtracted, flat-field-corrected, cleaned of cosmic rays, corrected for bad pixels and columns, and wavelength-calibrated using standard MIDAS,⁸ as described in ADC03. The line-of-sight velocity, velocity dispersion, and the higher order moments were measured from the galaxy absorption features present in the wavelength range centered on the Mg line triplet ($\lambda\lambda 5164, 5173, 5184$), using the Fourier Correlation Quotient method (Bender 1990; Bender et al. 1994).

In Figure 7 we compare the slit spectrum velocity and dispersion data with data extracted from our RFP two-dimensional maps in a $1''.0$ wide pseudoslit along the major axis, smoothing along the pseudoslit to match the slit spectrum smoothing. There is a zero-point offset of 14 km s^{-1} between the two velocity data sets, which has been added to the plotted data. The two data sets agree well, with very similar amplitudes and shapes of the rotation curves. A χ^2 analysis suggests that the velocity uncertainties are underestimated and that an additional uncertainty of 8.4 km s^{-1} should be added in quadrature to the error estimates. If all this additional uncertainty is assigned to the RFP data, the typical uncertainty of our velocity

⁸ MIDAS is developed and maintained by the European Southern Observatory.

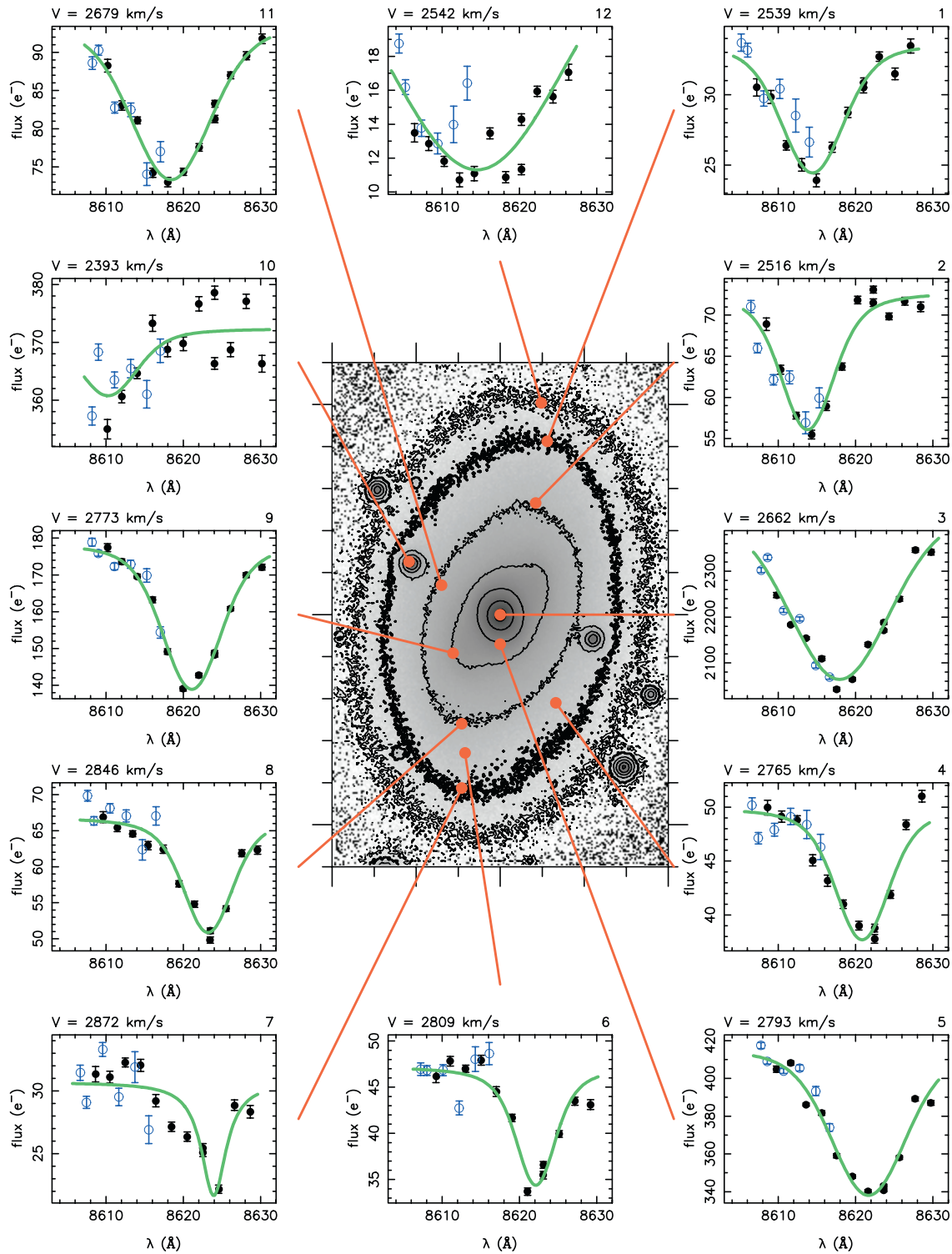


FIG. 6.—Sample profile fits; each fit-panel (numbered in its upper right and with the resulting V_{los} indicated at its upper left) points to the location in the galaxy (here shown by the I -band map from Fig. 1) for which it applies. The data points indicate the fluxes (in electrons) in the reduced data cube, while the green lines show our fitted profiles. The points are coded by the time order in which they were observed: the black points are the first 12 observed, while the blue points are the last six observed.

measurements is 12 km s^{-1} ; if the additional uncertainty is divided evenly between the two data sets, the typical RFP errors are 10 km s^{-1} (and typical slit spectrum errors are 8 km s^{-1}). The RFP velocity dispersion data have more scatter and larger estimated errors than the slit velocity dispersions. As noted above, we expect the lack of sufficient wavelength coverage to

affect the precision of the RFP dispersion measurements when the dispersions are large, as in most of the points along the pseudoslit. Nonetheless, the two data sets are in good general agreement, tracing similar amplitudes and distributions of the velocity dispersion. Again, a χ^2 analysis suggests that the uncertainties are underestimated and that an additional

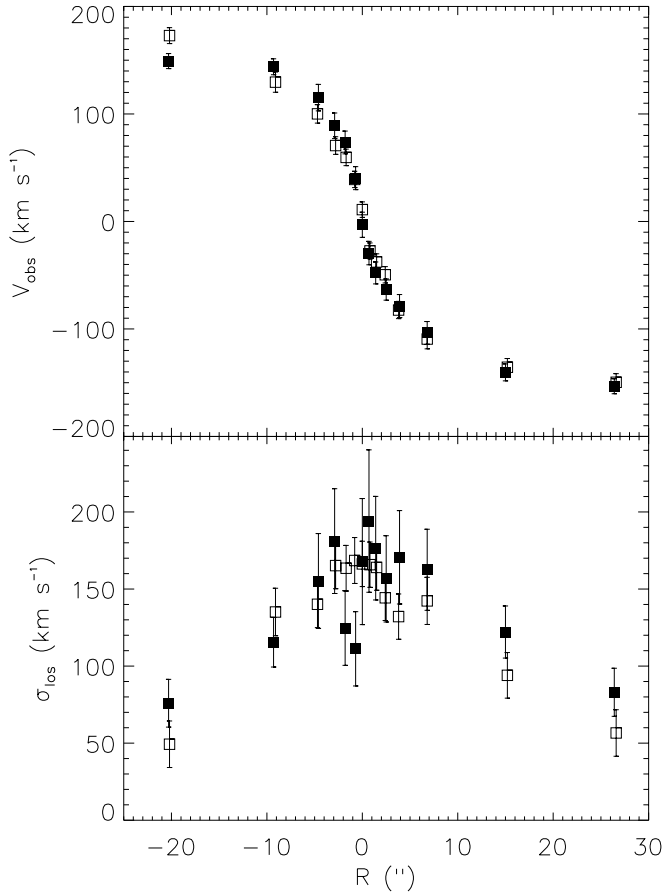


FIG. 7.—Comparison of our data with slit data. The top panel shows line-of-sight velocities, while the bottom one shows the velocity dispersions. The open symbols are slit data, and the solid symbols are the RFP data. The error bars correspond to 1σ deviations.

uncertainty of 20.1 km s^{-1} should be added in quadrature to the error estimates. If all this additional error is assigned to the RFP measurements, their typical precision is 31 km s^{-1} ; if the additional error is split equally between the two data sets, the RFP uncertainties are 27 km s^{-1} and the slit spectra errors are 15 km s^{-1} . There is some marginal indication that the velocity dispersions measured with the RFP are systematically larger than with the slit spectrograph. The mean difference of all the measurements is 8 km s^{-1} , and the mean difference of the measurements at radial distances greater than $7''$ (where the RFP profiles are adequately sampled) is 15 km s^{-1} ; these biases are smaller than the estimated uncertainties, and the spectral resolution of the RFP (corresponding to an instrumental dispersion of 64 km s^{-1}) makes precision measurements of dispersions below 50 km s^{-1} problematic.

Since the RFP and slit spectrograph data attain comparable results and accuracies, it is straightforward to compare the relative efficiencies of the two methods. Since the spectral resolution of this spectrograph was about 2.2 times better than that of the RFP, it should have been possible to widen the slit to $2''$ and still measure velocities with accuracies comparable to the RFP. In an 1800 s exposure, the spectrographic data reached to a limiting radius of $20''$, while the RFP data extended to $40''$, about 1.3 mag fainter. The total RFP exposure time was $18 \times 900 \text{ s}$. The sky and galaxy flux levels were sufficiently high that both instruments were in the photon noise limit regime. Thus, taking into account the telescope

apertures and the noise from the sky background, a single-slit spectrogram with $2''$ slit would reach the same surface brightness about 3.3 times faster than the RFP. However, the RFP data extend out to $\pm 20''$ along the galaxy minor axis; to cover this same area would require 20 spectrographic exposures. Thus the RFP is approximately 6 times more efficient than a slit spectrograph for measuring the two-dimensional velocity field of this galaxy.

We therefore conclude that the RFP data is in good agreement with the slit spectrum data and that the RFP technique affords a reliable means for obtaining absorption-line galaxy kinematics with significantly greater efficiency than standard slit spectroscopy.

5. KINEMATICS AND BAR PATTERN SPEED

5.1. The Rotation Curve

Using the velocity field data, we obtained the stellar mean rotation velocity curve, $V_*(R)$, by fitting tilted-rings (Begeman 1987, Palunas 1996), with the galaxy center, inclination and P.A._{disk} fixed to the values found in the photometry. We started by determining the systemic velocity, V_{sys} , obtaining $V_{\text{sys}} = 2670 \pm 4 \text{ km s}^{-1}$. This is in good agreement with Lauberts & Valentijn (1989), who obtained $V_{\text{sys}} = 2670 \pm 25 \text{ km s}^{-1}$, and with the averaged values of Bettoni & Galletta (1997), $V_{\text{sys}} = 2678 \pm 35 \text{ km s}^{-1}$. This parameter was then also fixed and $V_*(R)$ determined using pixels at angle $|\phi| \leq 45^\circ$ from the disk major axis in the intrinsic galaxy frame. The result is shown in Figure 8. Subtracting $V_*(R)$ from the velocity map produced small residuals, mostly $\leq 20 \text{ km s}^{-1}$ except near the bright foreground stars.

To determine the rotation curve of the galaxy we needed to correct for the asymmetric drift, a procedure that is somewhat uncertain. The asymmetric drift equation for the circular velocity, V_c , is (e.g., Binney & Tremaine 1987 eq. [4.33])

$$V_c^2 - V_*^2 = -\sigma_R^2 \left[\frac{\partial \ln \rho}{\partial \ln R} + \frac{\partial \ln \sigma_R^2}{\partial \ln R} + \left(1 - \frac{\sigma_\phi^2}{\sigma_R^2} \right) \right], \quad (2)$$

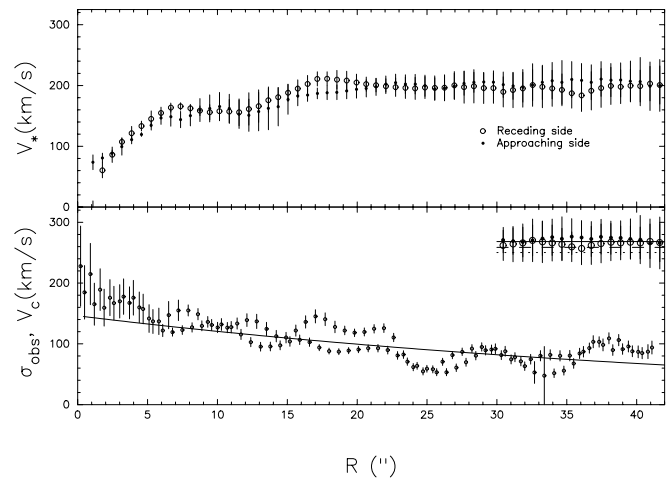


FIG. 8.—Observed stellar streaming velocities, V_* , (top) and the asymmetric drift analysis for the amplitude of the rotation curve (bottom). The bottom panel shows the observed velocity dispersion along the major axis of the disk; the best-fit exponential is indicated by the solid line. In the upper right corner of the lower panel are shown estimates of $V_{c,\text{flat}}$ (see eq. [2]) for $\alpha = 0.7$ (closed and open circles) at $R \geq 30''$. The radial average for this α is indicated by the solid horizontal line. The dashed and dotted horizontal lines indicate the radial averages obtained by assuming $\alpha = 0.85$ and $\alpha = 1.0$, respectively.

where ρ is the disk's volume density, and σ_ϕ and σ_R are the tangential and radial velocity dispersions in the cylindrical coordinates of the galaxy's intrinsic plane. To proceed further, we needed to make a number of assumptions. Following ADC03, we assumed that the rotation curve is flat at large radii and that both σ_{obs} and ρ decrease exponentially with radius. Thus the asymmetric drift equation becomes

$$V_{c,\text{flat}}^2 = V_*^2 + \frac{[\sigma_0 \exp(-R/R_\sigma)]^2}{\sin^2 i (1 + 2\alpha^2 \cot^2 i)} \left[2R \left(\frac{1}{R_d} + \frac{2}{R_\sigma} \right) - 1 \right], \quad (3)$$

where $\alpha = \sigma_z/\sigma_R$, σ_0 and R_σ are the parameters of the exponential fit to the observed major-axis velocity dispersion profile, and R_d is the exponential scale-length of the surface density. As in ADC03, we use three values of $\alpha = 0.7, 0.85$ and 1.0 , appropriate for early-type galaxies (Gerssen et al. 1997, 2000).

In Figure 8 we present this asymmetric drift correction to points at $R > 30''$. We used $R_d = 17''$ from the photometry, as appropriate for the region of interest, and fitted an exponential to σ_{obs} along a 7 pixel-wide slit on the major axis. We found a circular velocity amplitude, $V_{c,\text{flat}} = 256_{-15}^{+17}$ km s⁻¹. The radially averaged mean streaming velocity in the same radial range is $\bar{V}_* = 200 \pm 5$ km s⁻¹.

5.2. The Pattern Speed of NGC 7079

We calculated the TW integrals for NGC 7079 in nine strips in the ranges $-14'' \leq Y \leq -2''$ and $2'' \leq Y \leq 11''$. The limits on large $|Y|$ were chosen to avoid contamination by the bright stars flanking NGC 7079 near its the minor axis. The limits on small $|Y|$ were chosen to avoid a small (<1 pixel) offset between the kinematic and photometric centers, to which \mathcal{V} is sensitive because of the centrally peaked light distribution. In our standard case, we calculated the integrals inside an ellipse of semimajor axis, $A_{\text{max}} = 35''$, which does not quite reach the axisymmetric part of the disk (see Fig. 3), but where the surface brightness is more than 5 mag below the central value (compare D03). We chose the function $h(Y)$ for each integral to be the integrated surface brightness within the strip. We obtained error estimates for \mathcal{V} from 100 Monte Carlo realizations, where the observed velocity field was modified at each point by adding a velocity randomly drawn from a Gaussian distribution of width equal to the estimated velocity uncertainty at that point plus an additional 8.4 km s⁻¹ added in quadrature to account for the possible underestimate of the velocity uncertainty. In the standard case, we used for $\Sigma(X, Y)$ the *I*-band map; to match the photometric and kinematic maps, we first convolved the former to the seeing of the latter, then used several of the stars in the field of both maps to compute a geometric transformation between them. This transformation required only a translation and a single scale for X and Y , with no rotation or shear. The results for the standard case are shown in Figure 9; the best-fitting slope is -6.5 ± 0.1 km s⁻¹ arcsec⁻¹ (the negative sign here reflects only on our arbitrary choice of positive X).

We checked that this value is not sensitive to various choices we made. We first tested that using the *I*-band photometry has not biased our result by using instead an image generated by summing all the RFP frames. The resulting slope was -6.3 ± 0.3 km s⁻¹ arcsec⁻¹, in good agreement with the standard case. We also checked that our limits on the integrals are reasonable by confirming convergence of the values of \mathcal{X}

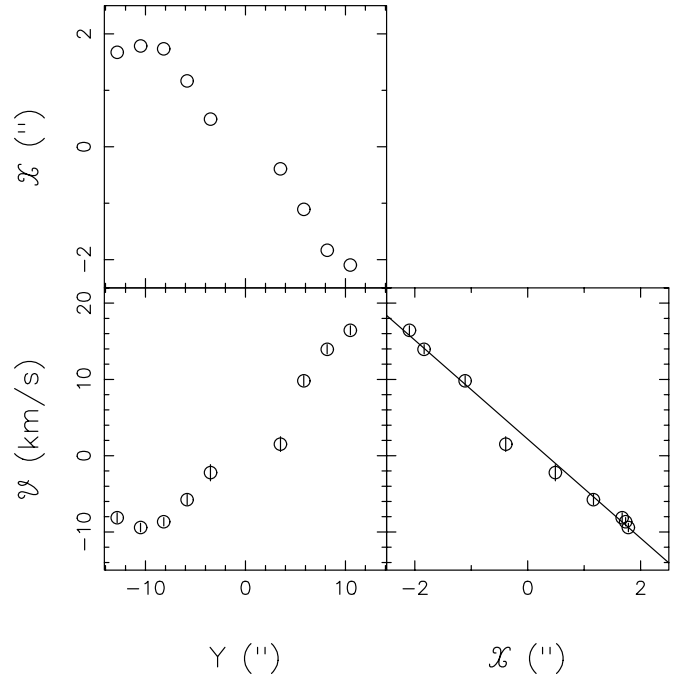


FIG. 9.—Integrals \mathcal{X} (top left) and \mathcal{V} (bottom left) plotted as a function of Y . The bottom right panel plots \mathcal{V} vs. \mathcal{X} ; fitting a straight line gives slope -6.5 ± 0.1 km s⁻¹ arcsec⁻¹ and $\chi^2 = 2.2$. Excluding the most discrepant point reduces χ^2 to 0.7 without changing the slope or its error significantly.

and \mathcal{V} when we changed the semimajor axis, A_{max} , of the ellipse within which the integrals were performed. In the range $31'' \leq A_{\text{max}} \leq 38''$, the variations in \mathcal{V} are all within the standard errors. We use the variations in \mathcal{X} in $35'' \leq A_{\text{max}} \leq 38''$ to define the errors in \mathcal{X} ; these small errors lead to negligible change in the value of the fitted slope and its uncertainty.

From this slope we calculate $\Omega_p = 8.4 \pm 0.2$ km s⁻¹ arcsec⁻¹ and $D_L = V_{c,\text{flat}}/\Omega_p = 30'' 6_{-1.3}^{+1.4}$ (67% confidence interval). We then find that $\mathcal{R} = V_{c,\text{flat}}/(a_B \Omega_p) = 1.2 \pm 0.1$ at the 67% confidence interval and $\mathcal{R} = 1.2_{-0.2}^{+0.3}$ at the 99% confidence interval, where we obtained the uncertainties by Monte Carlo experiments in which we varied $V_{c,\text{flat}}$ and a_B uniformly in their error intervals and Ω_p assuming Gaussian errors. At a probability of higher than 94%, NGC 7079 has a fast bar. Note that if the RFP overestimates the velocity dispersions in the region of interest, then the real \mathcal{R} would be even lower; in the limiting (and unphysical) case that velocity dispersions are negligible in the region of interest, we obtain $\mathcal{R} = 0.9 \pm 0.1$.

5.3. Variations in P.A._{disk}

Our two-dimensional data also allowed us to study the effects of errors in P.A._{disk} on the fitted slope. In the convention where the error in P.A._{disk}, $\delta_{\text{P.A.}}$, moves P.A._{disk} away from alignment with the bar when $\delta_{\text{P.A.}}$ is positive (the same convention as in D03), we repeated our standard TW measurement as before but for $-10^\circ \leq \delta_{\text{P.A.}} \leq 10^\circ$. The results, plotted in Figure 10, reveal that the slope is quite sensitive to rather small $\delta_{\text{P.A.}}$. Errors in P.A._{disk} of order 5° , for example, produce large errors in Ω_p , $\sim 50\%$ – 100% . Clearly, how accurately Ω_p can be measured depends strongly on how well P.A._{disk} can be determined. Our high-precision determination of P.A._{disk} (see Fig. 3) allows us to determine Ω_p with the small uncertainty

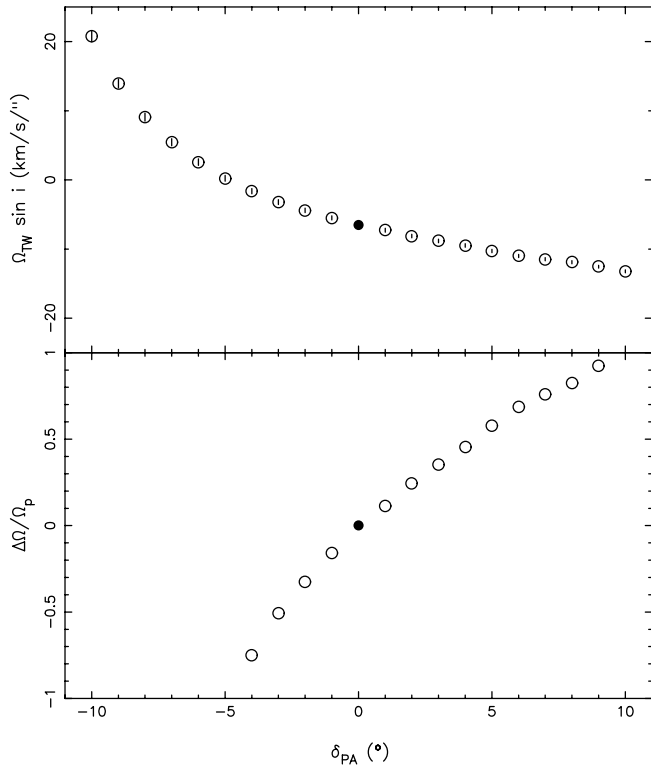


FIG. 10.—Slope of the best-fitting line (*top*) and the resulting error in Ω_{TW} , the pattern speed derived from the linear regression of the TW integrals (*bottom*), as functions of error in disk P.A., $\delta_{P.A.}$. In the bottom panel, $\Delta\Omega/\Omega_p \equiv (\Omega_{TW} - \Omega_p)/\Omega_p$. The solid circle in both panels represents the case when $\delta_{P.A.} = 0$.

quoted above. Note, however, that had we used the value of $P.A._{disk}$ from RC3, our value of Ω_p would have been some 35% larger.

These results are consistent with those of D03, who studied $\Delta\Omega/\Omega_p$ systematically by means of an N -body simulation. The sensitivity of Ω_p calculated here from the NGC 7079 observations is, if anything, somewhat larger than in D03 (compare our Fig. 10 with Fig. 9 in D03). Because $P.A._{disk}$ errors can also be produced by disk density ellipticities, D03 was able to show that such ellipticities had to be $\lesssim 0.07$ for the sample of SB0 galaxies with TW measurements.

6. DISCUSSION AND CONCLUSIONS

We have shown that FP techniques can measure galaxy kinematics from stellar absorption-lines in early-type galaxies. To the best of our knowledge, this is the first successful demonstration of this technique. Comparison with a traditional slit spectrogram along the major axis of the galaxy confirms the accuracy of the FP measurements. For the galaxy observed here, mapping the kinematics was about 6 times more efficient with the FP than with a slit spectrograph. For an object that fills more of the FP field of view, the advantage would be even greater. The fact that the spectral and spatial resolutions are decoupled with an imaging FP affords a great deal of flexibility in the data analysis, allowing extended measurements at lower spatial resolution in the faint outer regions of galaxies. Since the FP samples a large area on the sky, the determination and subtraction of the sky spectrum can be performed with high precision, again allowing measurement to fainter surface brightnesses. The full two-dimensional

format of FP kinematic maps permits unambiguous determination of the positions at which velocity samples are obtained and allows optimal extraction of information in crowded fields, which can be difficult with slit data.

There are some limitations to using a FP for absorption-line spectroscopy. The temporal sampling of the spectrum limits the accuracy of reconstruction of the line profile; this is the reason why we did not pursue measurement of higher order moments of the velocity distribution function. The next generation RFP, with a built-in transparency monitor, should help alleviate this difficulty. The reduction of FP data has a reputation for difficulty; we believe that this is more due to the wealth of information available in a full two-dimensional kinematic data set than to the inherent difficulty of analyzing the FP data. Nonetheless, the techniques for handling FP data are not widely known, and FP software is neither as generally available nor as robust as the packages for slit spectroscopy. Finally, while we have shown the significant efficiency of a FP for producing a full two-dimensional map of the stellar kinematics of a galaxy, there are many classes of investigation for which such extensive data are not required. In such situations traditional slit spectroscopy is both simpler and more efficient.

These problems should not, however, be overstated. The promise of FP absorption-line spectroscopy is demonstrated by the results obtained here. This is the tightest bound on \mathcal{R} ever obtained on a barred galaxy using the TW method, with a 67% interval less than half that for the next best published case (ESO 139–G009; ADC03). More dramatically, the fractional uncertainty on Ω_p is less than 3%: typical uncertainties from slit spectroscopy are $\sim 20\%–30\%$.

We showed that in order to measure Ω_p to such high precision, the P.A. of the disk needs to be known quite accurately. Our’s is the first demonstration on a real galaxy that the TW method is sensitive to small errors in P.A. For NGC 7079, we were able to measure $P.A._{disk}$ to better than 1° . But if we had relied on the RC3 value of $P.A._{disk}$, we would have obtained a value of $\Omega_p \sim 35\%$ larger.

We found, at high confidence, a fast bar in NGC 7079. As in all previous measurements with good precision, the probability that $\mathcal{R} = 1.7$ is low: if we assume extreme values for a_B and $V_{c,flat}$ to maximize \mathcal{R} , we find that $\mathcal{R} = 1.7$ requires $\Omega_p = 7.3 \text{ km s}^{-1} \text{ arcsec}^{-1}$, or over 5σ smaller than our measured value. Such fast bars continue to be a challenge for cuspy cold dark matter halos.

We thank the CTIO staff for their excellent support and for troubleshooting instrument problems during the observing run. We thank Povilas Palunas for providing us with his tilted-rings velocity-field fitter. We especially would like to thank Enrico Maria Corsini for the spectrum and reduced kinematics along the major axis. V. P. D. thanks J. A. L. Aguerri for useful discussions and cross-checks. V. P. D. acknowledges support by NSF grant AST 96-17088 and the Swiss National Science Foundation grants 20-56888.99 and 20-64856.01. T. B. W. acknowledges support by NSF grants AST 97-31052 and AST 00-98650. The RFP was developed with support from Rutgers University and the NSF, under grant AST 83 19-344. We dedicate this paper to the memory of Bob Schommer, who was instrumental in developing the RFP, turning it into a user instrument at CTIO, and producing much excellent science with it.

REFERENCES

- Aguerri, J. A. L., Debattista, V. P., & Corsini, E. M. 2003, *MNRAS*, 338, 465 (ADC03)
- Aguerri, J. A. L., Muñoz-Tuñón, C., Varela, A. M., & Prieto, M. 2000, *A&A*, 361, 841
- Athanassoula, E. 1992, *MNRAS*, 259, 345
- Bacon, R., et al. 2001, *MNRAS*, 326, 23
- Beauvais, C., & Bothun, G. 2001, *ApJS*, 136, 41
- . 1999, *ApJS*, 125, 99
- Beers, T. C., Flynn, K., & Gebhardt, K. 1990, *AJ*, 100, 32
- Begeman, K. 1987, Ph.D. thesis, Univ. Groningen
- Bettoni, D., & Galletta, G. 1997, *A&AS*, 124, 61
- Bender, R. 1990, *A&A*, 229, 441
- Bender, R., Saglia, R. P., & Gerhard, O. E. 1994, *MNRAS*, 269, 785
- Binney, J., & Tremaine, S. 1987, *Galactic Dynamics* (Princeton: Princeton Univ. Press)
- Bosma, A. 1981, *AJ*, 86, 1791
- Bottema, R. 1997, *A&A*, 328, 517
- Buta, R. 1995, *ApJS*, 96, 39
- Buta, R., & Purcell, G. B. 1998, *AJ*, 115, 484
- Buta, R., Purcell, G. B., Cobb, M. L., Crocker, D. A., Rautiainen, P., & Salo, H. 1999, *AJ*, 117, 778
- Buta, R., Ryder, S. D., Madsen, G. J., Wesson, K., Crocker, D. A., & Combes, F. 2001, *AJ*, 121, 225
- Contopoulos, G. 1980, *A&A*, 81, 198
- Corsini, E. M., et al. 1999, *A&A*, 342, 671
- Courteau, S., & Rix, H.-W. 1999, *ApJ*, 513, 561
- Debattista, V. P. 2003, *MNRAS*, 342, 1194 (D03)
- Debattista, V. P., Corsini, E. M., & Aguerri, J. A. L. 2002, *MNRAS*, 332, 65
- Debattista, V. P., & Sellwood, J. A. 2000, *ApJ*, 543, 704
- . 1998, *ApJ*, 493, L5
- de Vaucouleurs, G., de Vaucouleurs, A., Corwin, H. G., Buta, R. J., Paturel, G., & Fouqué, P. 1991, *Third Reference Catalogue of Bright Galaxies* (New York: Springer)
- Eskridge, P. B., et al. 2000, *AJ*, 119, 536
- Freeman, K. C. 1970, *ApJ*, 160, 811
- Garcia, A. M. 1993, *A&AS*, 100, 47
- Gebhardt, K., Pryor, C., Williams, T. B., & Hesser, J. E. 1995, *AJ*, 110, 1699
- . 1994, *AJ*, 107, 2067
- Gebhardt, K., Pryor, C., Williams, T. B., Hesser, J. E., & Stetson, P. B. 1997, *AJ*, 113, 1026
- Gerhard, O. E. 1993, *MNRAS*, 265, 213
- Gerssen, J., Kuijken, K., & Merrifield, M. R. 1997, *MNRAS*, 288, 618
- . 1999, *MNRAS*, 306, 926
- Gerssen, J., Kuijken, K., & Merrifield, M. R. 2000, *MNRAS*, 317, 545
- . 2003, *MNRAS*, 345, 261
- Graham, J. A. 1982, *PASP*, 94, 244
- Hamuy, M., Walker, A. R., Suntzeff, N. B., Gigoux, P., Heathcote, S. R., & Phillips, M. M. 1992, *PASP*, 104, 533
- Hernquist, L., & Weinberg, M. D. 1992, *ApJ*, 400, 80
- Hubble, E. 1926, *ApJ*, 64, 321
- Kalnajs, A. J. 1983, in *Internal Kinematics and Dynamics of Galaxies*, ed. E. Athanassoula (Dordrecht: Reidel), 87
- Kent, S. M. 1986, *AJ*, 91, 1301
- Knapen, J. H. 1999, in *ASP Conf. Ser. 187, The Evolution of Galaxies on Cosmological Timescales*, ed. J. E. Beckman, & T. J. Mahoney (San Francisco: ASP), 72
- Kranz, T., Slyz, A., & Rix, H.-W. 2001, *ApJ*, 562, 164
- Lauberts, A., & Valentijn, E. A. 1989, *The Surface Photometry Catalogue of the ESO-Uppsala Galaxies* (Garching bei München: ESO)
- Lindblad, P. A. B., Lindblad, P. O., & Athanassoula, E. 1996, *A&A*, 313, 65
- Little, B., & Carlberg, R. G. 1991, *MNRAS*, 250, 161
- Merrifield, M. R., & Kuijken, K. 1995, *MNRAS*, 274, 933
- Narayan, C. A., & Jog, C. J. 2003, *A&A*, 407, L59
- O'Neill, J. K., & Dubinski, J. 2003, *MNRAS*, 346, 251
- Osterbrock, D. E., Fulbright, J. P., Martel, A. R., Keane, M. J., Trager, S. C., & Basri, G. 1996, *PASP*, 108, 277
- Palunas, P. 1996, Ph.D. thesis, Rutgers Univ.
- Palunas, P., & Williams, T. B. 2000, *AJ*, 120, 2884
- Pohlen, M., Dettmar, R.-J., Lütticke, R., & Aronica, G. 2002, *A&A*, 392, 807
- Rubin, V. C., Ford, W. K., & Thonnard, N. 1980, *ApJ*, 238, 471
- Schlegel, D. J., Finkbeiner, D. P., & Davis, M. 1998, *ApJ*, 500, 525
- Tremaine, S., & Ostriker, J. P. 1999, *MNRAS*, 306, 662
- Tremaine, S., & Weinberg, M. D. 1984, *ApJ*, 282, L5
- Valenzuela, O., & Klypin, A. 2003, *MNRAS*, 345, 406
- van Albada, T. S., & Sancisi, R. 1986, *Phil. Trans. R. Soc. London A*, 320, 447
- van der Kruit, P. C. 1995, in *IAU Symp. 164, Stellar Populations*, ed. P. C. van der Kruit & G. Gilmore (Dordrecht: Kluwer), 205
- . 1979, *A&AS*, 38, 15
- van der Marel, R. P., & Franx, M. 1993, *ApJ*, 407, 525
- Verolme, E. K., et al. 2002, *MNRAS*, 335, 517
- Weiner, B. J., Sellwood, J. A., & Williams, T. B. 2001b, *ApJ*, 546, 931
- Weiner, B. J., Williams, T. B., van Gorkom, J. H., & Sellwood, J. A. 2001a, *ApJ*, 546, 916
- Weinberg, M. D. 1985, *MNRAS*, 213, 451
- Weinberg, M. D., & Katz, N. 2002, *ApJ*, 580, 627